

A neutron diffraction study of the hydrous borate inderborite, $\text{CaMg}[\text{B}_3\text{O}_3(\text{OH})_5]_2(\text{H}_2\text{O})_4 \cdot 2\text{H}_2\text{O}$

G. DIEGO GATTA^{1,*}, ENRICO CANNAÒ¹, DAVIDE COMBONI¹, TOMMASO BATTISTON¹, AND OSCAR FABELLO²

¹Dipartimento di Scienze della Terra, Università degli Studi di Milano, Via Botticelli 23, I-20133 Milano, Italy

²Institut Laue-Langevin, 71 Avenue des Martyrs, F-38000 Grenoble, France

ABSTRACT

The crystal chemistry of inderborite, a B-rich mineral (B_2O_3 ~41 wt%) with ideal formula $\text{CaMg}[\text{B}_3\text{O}_3(\text{OH})_5]_2 \cdot 6\text{H}_2\text{O}$ or $\text{CaMg}[\text{B}_3\text{O}_3(\text{OH})_5]_2(\text{H}_2\text{O})_4 \cdot 2\text{H}_2\text{O}$ from the Inder Deposit, Kazakhstan, was re-investigated by a multi-methodological approach (single-crystal X-ray and neutron diffraction, electron probe micro-analysis in wavelength-dispersive mode, laser ablation multi-collector inductively mass spectrometry). The experimental findings show that the real chemical formula of inderborite from the Inder Deposit is virtually identical to the ideal one: the fraction of potential isomorphous substituents is insignificant. Boron is, therefore, the only industrially relevant element occurring in this mineral. The in situ B isotope composition of the Inder inderborite shows enrichment in the heavy ^{11}B isotope, giving a weighted mean $\delta^{11}\text{B}_{\text{NIST951}}$ of $+35.15 \pm 0.49$ ‰ (2σ , $N = 6$). Such a positive $\delta^{11}\text{B}$ value falls within the range of values in which the source of boron is ascribable to marine reservoirs rather than to terrestrial ones.

X-ray (at 293 K) and neutron (at 20 K) structure refinements confirm that the principal building block unit of the structure is a $[\text{B}_3\text{O}_3(\text{OH})_5]^{2-}$ ring, consisting of two $\text{BO}_2(\text{OH})_2$ tetrahedra (B-ion in sp^3 electronic configuration) and one planar-triangular BO_2OH group (B-ion in sp^2 electronic configuration). In the $[\text{B}_3\text{O}_3(\text{OH})_5]^{2-}$ ring, all the oxygen atoms that are not shared between two boron atoms are protonated. The building units share corners with the $\text{CaO}_2(\text{OH})_4(\text{OH}_2)_2$ polyhedra and $\text{Mg}(\text{OH})_4(\text{OH}_2)_2$ octahedra, forming hetero-polyhedral sheets parallel to (100). Subsequent hetero-polyhedral sheets are mutually connected only by H-bonding interactions, even mediated by the zeolitic (“interstitial”) H_2O molecules. Ten out of 11 independent oxygen sites in the structure of inderborite are involved in H-bonds as donors or acceptors, and this reflects the pervasive effect of the H-bonding network. The role played by the complex H-bond network is expected to be substantial on the stability of the crystalline edifice, having effects within the single hetero-polyhedral sheet, between subsequent sheets, and in the bonding with the interstitial zeolitic H_2O molecules. Finally, the potential utilizations of inderborite, as a B-bearing mineral, are discussed.

Keywords: Inderborite, borates, mineral commodity, X-ray diffraction, neutron diffraction, crystal chemistry, hydrogen bonding

INTRODUCTION

Inderborite is a hydrous borate, with ideal chemical formula $\text{CaMg}[\text{B}_3\text{O}_3(\text{OH})_5]_2 \cdot 6\text{H}_2\text{O}$, found in lacustrine borate deposits or in the caprock of salt diapers, usually coexisting with other common borates, such as borax $\{\text{Na}_2[\text{B}_4\text{O}_5(\text{OH})_4] \cdot 8\text{H}_2\text{O}\}$, ulexite $\{\text{NaCa}[\text{B}_5\text{O}_6(\text{OH})_6] \cdot 5\text{H}_2\text{O}\}$, colemanite $\{\text{Ca}[\text{B}_3\text{O}_4(\text{OH})_3] \cdot \text{H}_2\text{O}\}$, hydroboracite $\{\text{CaMg}[\text{B}_3\text{O}_4(\text{OH})_3]_2 \cdot 3\text{H}_2\text{O}\}$, kurnakovite $[\text{MgB}_3\text{O}_3(\text{OH})_5 \cdot 5\text{H}_2\text{O}]$, inderite $[\text{MgB}_3\text{O}_3(\text{OH})_5 \cdot 5\text{H}_2\text{O}]$, and pinnoite $\{\text{Mg}[\text{B}_2\text{O}(\text{OH})_6]\}$. The type locality of this mineral is the Inder borate deposit, Kazakhstan. Inderite contains boron as an essential component (more than 41 wt% B_2O_3) and, along with the other hydrous borates from lacustrine deposits, they represent more than 90% of the B-rearing minerals utilized by industry worldwide. The global demand for borates has drastically increased during the last 20 years, and the market is expected to grow in the near future to accommodate the rising demand of B

in a series of technologically relevant products (e.g., ceramics and refractory materials, heat-resistant glasses, fire retardants, radiation-shielding materials, B-alloy steels, pharmaceutical products, soaps and detergents, and agricultural compounds) (source: USGS Mineral Commodity Summaries, <https://www.usgs.gov/centers/national-minerals-information-center/mineral-commodity-summaries>; British Geological Survey, Centre for Sustainable Mineral Development, <https://www2.bgs.ac.uk/mineralsuk/>). Due to its high supply risk and economic importance, boron is among the critical elements included in the “critical raw materials” list according to the European Commission 2023 (https://ec.europa.eu/commission/presscorner/detail/en/ip_23_1661).

In the last years, we have re-investigated the crystal structure and physical and chemical stability (at high/low-temperature and high-pressure conditions or in response to leaching) of a series of borates: colemanite (Lotti et al. 2017, 2018, 2019); kurnakovite (Gatta et al. 2019; Pagliaro et al. 2021); kernite $[\text{Na}_2\text{B}_4\text{O}_6(\text{OH})_2 \cdot 3\text{H}_2\text{O}]$ (Comboni et al. 2020a; Gatta et al. 2020); meyerhofferite $\{\text{Ca}_2[\text{B}_6\text{O}_6(\text{OH})_{10}] \cdot 2\text{H}_2\text{O}\}$ (Comboni et al. 2020b;

* Corresponding author E-mail: diego.gatta@unimi.it. Orcid <https://orcid.org/0000-0001-8348-7181>

Gatta et al. 2022a); inyoite $[\text{CaB}_3\text{O}_3(\text{OH})_5 \cdot 4\text{H}_2\text{O}]$ (Comboni et al. 2022); probertite $\{\text{CaNa}[\text{B}_5\text{O}_7(\text{OH})_4] \cdot 3\text{H}_2\text{O}\}$ (Gatta et al. 2022b); and inderite (Comboni et al. 2023) by a multi-methodological approach. Our experiments were aimed to search for potential B-rich aggregates in construction materials (e.g., Portland or Sorel cements) due to the efficient radiation-shielding capacity of ^{10}B [its high cross section for the $^{10}\text{B}(n,\alpha)^7\text{Li}$ reaction is ~ 3840 barns (Carter et al. 1953; Sears 1986; Palmer and Swihart 1996; Rauch and Waschkowski 2002)]. The neutron absorption capacity of ^{11}B is, on the other hand, modest (cross-section ~ 0.006 barns), but in natural borates about 20% of boron occurs as ^{10}B . Following the previous experiments, the aim of this paper is to extend our systematic study on borates to inderborite, among the natural borates with the highest B-content (~ 41 wt% B_2O_3). Here, we report the experimental findings based on single-crystal X-ray (at 298 K) and neutron diffraction (at 20 K), electron microprobe analysis in wavelength-dispersive mode (EPMA-WDS), and laser ablation inductively mass spectrometry (LA-ICP-MS) and LA multi-collector ICP-MS (LA-MC-ICP-MS). The results provide (1) the chemical composition of this mineral (unveiling major, minor, and trace elements) and its B isotopic composition, and (2) a structural model based on modern standards, with the location of all the H sites, their vibrational regime and the description of the complex and pervasive H-bonding net (inderborite contains up to ~ 39 wt% of total H_2O), which is presumed to play a substantial role in the thermal and compressional stability of this mineral (currently under investigation), limiting its potential use as B-aggregate in concretes. Due to the high-B and -H content and the occurrence of millimetric gem-quality crystals, inderborite is a good candidate for a neutron diffraction investigation.

PREVIOUS STUDIES ON INDERBORITE

Inderborite was discovered as a new mineral species by Gorshkov (1941) at the Lower Permian gypsum beds in the Inder mountains, northwards from Lake Inder, Guriev region, Kazakhstan, in paragenesis with other already known (at that time) hydrous borates: colemanite, ulexite and, inyoite. The first crystallographic data collected by Gorshkov (1941) suggested that the mineral was monoclinic (with a ratio among unit-cell edges of $a:b:c = 1.6346:1:1.3173$ and a monoclinic angle of $\beta = 90^\circ 48'$), and the first (wet) chemical characterization led to the ideal formula $\text{CaO} \cdot \text{MgO} \cdot 3\text{B}_2\text{O}_3 \cdot 11\text{H}_2\text{O}$ (or $\text{CaMgB}_6\text{O}_{11} \cdot 11\text{H}_2\text{O}$). Independently, but slightly later in the same year, Ikornikova and Godlevsky (1941) reported a new mineral species (proposed name: metahydroboracite), but their chemical and crystallographic data were virtually identical to those previously reported by Gorshkov (1941) for inderborite. The name assigned to the new mineral was, therefore, inderborite (Fleischer 1943). Later, the crystal structure of inderborite, from the type locality in Kazakhstan, was solved and refined by Kurkutova et al. (1966), on the basis of two-dimensional photographic X-ray single-crystal data. The structure model was described in the space group $C2/c$ and, despite consistent at a first approximation, was provided without any H sites and with a poor agreement factor (R -factor). A better model was later provided by Burns and Hawthorne (1994), on the basis of a high-quality single-crystal X-ray structure refinement, with a first assignment of 11 independent H sites. The space group was confirmed to be $C2/c$,

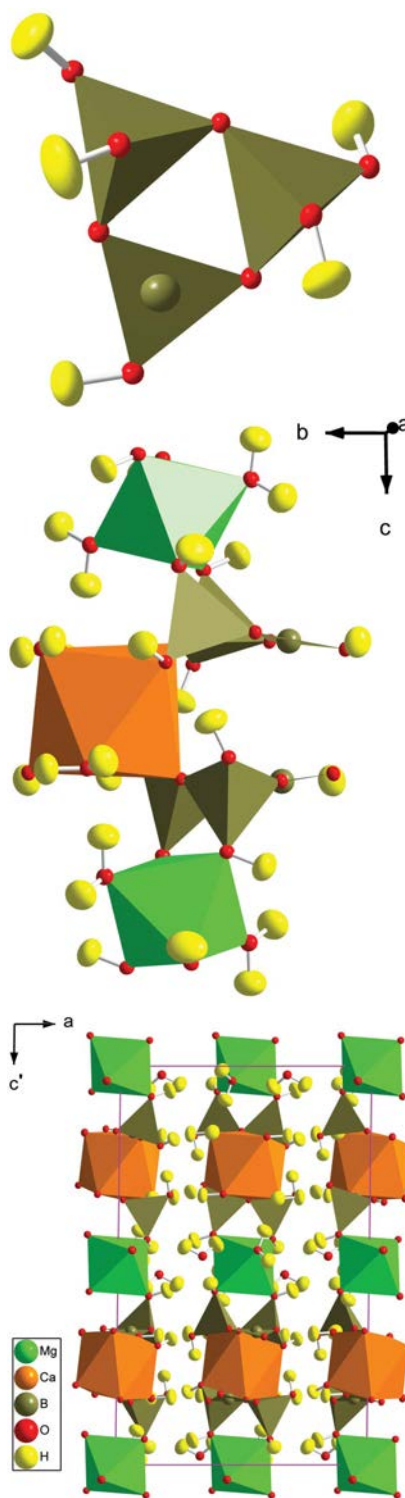


FIGURE 1. The principal building block unit {made by the $[\text{B}_3\text{O}_3(\text{OH})_5]^{2-}$ ring}, a fragment of the hetero-polyhedral sheets parallel to (100) (made by the building block units connected to Ca- and Mg-polyhedra) and a view down [010] of the crystal structure of inderborite. Structure model is based on the neutron structure refinement of this study (intensity data collected at 20 K). Displacement ellipsoid probability factor: 90%. Atomic site labels are same in Figure 2. (Color online.)

with unit-cell parameters $a \sim 12.137$, $b \sim 7.433$, $c \sim 19.234$ Å, and $\beta \sim 90.3^\circ$, and the crystallographically derived chemical formula was given as: $\text{CaMg}[\text{B}_3\text{O}_3(\text{OH})_5]_2(\text{H}_2\text{O})_4 \cdot 2\text{H}_2\text{O}$ ($Z = 4$). The principal building block unit of the inderborite structure (also called “fundamental building block” unit by Burns and Hawthorne 1994) is a $[\text{B}_3\text{O}_3(\text{OH})_5]^{2-}$ ring, consisting of two B-tetrahedra and one planar-triangular B-unit (Fig. 1). The same building block unit occurs also in the structures of kurnakovite, meyerhofferite, inyoite, inderite, and solongoite (Hawthorne 2012). In the $[\text{B}_3\text{O}_3(\text{OH})_5]^{2-}$ ring, all the oxygen atoms that are not shared between two boron atoms are protonated (Burns and Hawthorne 1994). In inderborite, the building units share corners with the Ca-polyhedra and Mg-octahedra, forming hetero-polyhedral sheets parallel to (100), as shown in Figure 1. The role played by the complex H-bond network was expected to be substantial, having effects within the single building unit, between adjacent units, and in the bonding with the zeolitic H_2O molecules.

Despite the fact that the structure model of inderborite has been essentially unveiled, it is surprising that, in the literature, there is no data, based on modern standards, about the chemical composition of this mineral, especially for minor and trace elements. To date, the nature and role of potential substituents for Ca, Mg, B, and OH-group are completely unknown.

MATERIALS AND EXPERIMENTAL METHODS

Inderborite sample

The sample of inderborite investigated in this study was kindly provided by the late Renato Pagano (Italy), with ref. #8029 of his collection. The hand specimen is represented by some colorless, well-formed prismatic, millimetric crystals from the “Quarry 98,” Inder Deposit, Kazakhstan, in which inderborite coexists with other borates (e.g., borax, boracite, colemanite, inderite, inyoite, kurnakovite, pinnoite, preobrazhenskite, tirtskite, ulexite, volkovskite), sulfates (e.g., anhydrite, celestine, gypsum, thénardite, vanthoffite), halides-fluorides, carbonates (e.g., aragonite, calcite, dolomite), and silicates (mainly clay minerals). The borates at the Inder deposit are geologically connected to a Permian salt dome that intrudes Mesozoic and Cenozoic sediments, covering an area of about 100 sq. miles. Halides, sulfates, and clay minerals form the internal part of the salt dome, whereas the external part consists of a series of Permian gypsum-rich rocks with reddish clays interbedded with borates ores. A detailed description of the Inder deposit is provided by Pekov and Abramov (1993) and Pekov (1998).

Chemical characterization

The chemical composition of the inderborite sample of this study was first investigated by EPMA-WDS with a JEOL 8200 Super Probe system at the CO-SPECT UNITECH platform, University of Milan, with the following operating conditions: 15 kV and 5 nA, 5 μm beam diameter, 30 s of counting times on the peaks, and 10 s on the backgrounds. A series of minerals were used as standards; the results were corrected for matrix effects using a ZAF routine, as implemented in the JEOL suite of programs. The standards employed were forsterite-154 (Mg), fayalite-143 (Fe), grossular (Al, Si, Ca), K-feldspar (K), omphacite (Na), sanbornite (Ba), celestine (Sr), and apatite (F). The three millimetric crystals of inderborite under investigation were found to be homogeneous but with some micro-inclusions of quartz. Only Ca and Mg concentrations were measured at a significant level. The measured weight fractions of Ca and Mg were nominally identical to the ideal ones (within the e.s.d.), i.e., CaO 11.2(2) wt% and MgO 7.9(2) wt%. As commonly observed for hydrous borates (e.g., Gatta et al. 2022b), even in this case, a modest degeneration of the crystals was observed under the electron beam.

The in situ trace element concentration was determined using a laser ablation system (Analyte Excite ArF excimer 193 nm, Teledyne Photon Machines) coupled to a single-collector quadrupole ICP-MS (iCAP RQ, Thermo Fisher Scientific) hosted at the Geochemistry, Geochronology and Isotope Geology laboratory of the Earth Sciences Department, University of Milan (ESD-MI). The laser micro-probe system is equipped with an HelEx II volume chamber for a fast wash out of the ablated materials. Helium was used as the carrier gas with a flow rate of

TABLE 1. In situ trace element concentrations (in wt ppm, 1 σ) and in situ B isotope composition (in ‰, 2 σ) of inderborite, based on the LA-ICP-MS and LA-MC-ICP-MS data

Analyzed isotope	Analyte symbol	Average (N = 6)	1 σ
7	Li	<13.5	
9	Be	2.85	1.36
45	Sc	<9.97	
49	Ti	<29.53	
51	V	<3.31	
53	Cr	<52.37	
55	Mn	<8.05	
59	Co	<8.02	
60	Ni	<34.14	
65	Cu	<42.83	
66	Zn	<36.57	
75	As	21.1	6.4
85	Rb	<3.80	
88	Sr	35.6	43.4
89	Y	<0.25	
90	Zr	<0.38	
93	Nb	<0.64	
111	Cd	2.34	1.37
121	Sb	<2.55	
133	Cs	<1.21	
137	Ba	0.997	0.806
139	La	0.143	0.046
140	Ce	0.390	0.028
141	Pr	0.061	0.017
146	Nd	1.14	0.82
149	Sm	0.700	0.710
151	Eu	0.190	0.190
157	Gd	0.465	0.092
159	Tb	0.124	0.049
163	Dy	<0.001	
165	Ho	0.060	0.060
167	Er	<0.55	
169	Tm	0.037	0.077
173	Yb	<0.001	
175	Lu	0.078	0.079
177	Hf	<0.001	
181	Ta	0.053	0.035
182	W	0.450	0.410
208	Pb	1.43	0.61
232	Th	<0.001	
238	U	<0.125	
		Weighted mean (N = 6)	2 σ
	$\delta^{11}\text{B}$	+35.15	0.49

~ 0.5 L/min in the ablation cell and ~ 0.2 L/min in the HelEx II cup. The laser spot size was set to 65 μm , and a laser fluence of 2.0 J/cm², with a repetition rate of 7 Hz, was used. Each analysis consisted of 40 s of background signal, 60 s of laser signal, and 20 s of wash-out time. The NIST SRM 610 synthetic glass was used as primary external standard (Jochum et al. 2011) and ⁴³Ca was used as internal standard. Quality control was achieved by analyzing the USGS reference basaltic glass GSD-2g (Wilson 2018), the NIST SRM 612 (Jochum et al. 2011), and the IAEA-B6 obsidian (Tonarini et al. 2003) together with the unknown. Precision is better than 5% for most of the elements, and accuracy is within 10% of the reference values. Data reduction was carried out using the Glitter software package (Griffin et al. 2008). Data are listed in Table 1.

The in situ B isotope composition of the Inder inderborite was measured using the same laser ablation system used for the determination of the trace element concentrations, connected with a double-focusing multi-collector (MC-)ICP-MS (Neptune XT, Thermo Fisher Scientific) hosted at the ESD-MI. The measurements were performed in single spot mode with a laser fluence of 3.0 J/cm² of the sample surface, a repetition rate of 7 Hz, and a fixed spot size diameter of 40 μm . The He flow rates within the ablation cell and in the arm of the HelEx II were set to ~ 0.51 and ~ 0.24 L/min, respectively. The signal intensity of the ¹¹B and ¹⁰B were simultaneously acquired using two Faraday cups (H4 and L2, respectively) connected to 10¹¹ Ω amplifier resistors. The instrumentation was set up for the maximum sensitivity using 0.8 X-skimmer and 1.2 Ni-Jet sample cones and the Jet pump at the ICP interface. The isobaric interferences of ⁴⁰Ar⁺ and ²⁰Ne²⁺ on mass 10 were resolved at low-resolution mode. Each analysis consisted of 60 cycles of background followed by 80 cycles of data acquisition and 16 cycles of wash time, for a total of 156 cycles of ~ 0.5 s each. The results are reported in the common

delta(δ)-notation as per mil (‰) and expressed relative to the isotopic ratio of the NIST SRM 951 boric acid ($^{11}\text{B}/^{10}\text{B} = 4.04362 \pm 0.00137$, 2σ ; Catanzaro et al. 1970). Data reduction was carried out offline with an in-house spreadsheet; $^{11}\text{B}/^{10}\text{B}$ ratios exceeding 2σ have been discharged. No downhole isotope ratio fractionation was observed. Instrumental isotope fractionation was corrected using the sample-standard bracketing approach using the IAEA-B4 tourmaline (schorl) as the primary standard ($\delta^{11}\text{B} = -8.62 \pm 0.17$, 2σ ; Tonarini et al. 2003). Potential laser-induced isotope fractionation was evaluated by analyzing two dravitic tourmalines [SY309 and SY441 from Marschall et al. (2006)] and the B-rich synthetic andesitic glass ARM-2 [10 500 wt. ppm of B, Wu et al. (2021)] in the same analytical run with the Inder inderborite. Boron isotope compositions obtained for the dravitic tourmalines ($\delta^{11}\text{B}_{\text{SY441}} = +19.41 \pm 0.40$ ‰, 2σ , $N = 2$; $\delta^{11}\text{B}_{\text{SY309}} = +21.22 \pm 0.47$ ‰, 2σ , $N = 2$), and for the andesitic ARM-2 glass ($\delta^{11}\text{B} = -11.74 \pm 0.52$ ‰, 2σ , $N = 4$) agree with the published values. Further check for potential instrumental and laser-induced isotope fractionation were done by analyzing a new set of tourmaline standards (Schorl 112566, Dravite 108796, and Elbaite 98144) in a separate session at similar instrumental parameters and conditions and using the IAEA-B4 tourmaline as calibrating standard. The measured $\delta^{11}\text{B}$ values are -13.38 ± 0.15 ‰ (2σ , $N = 3$) for the Schorl 112566, -6.29 ± 0.02 ‰ (2σ , $N = 3$) for the Dravite 108796, and -12.11 ± 0.05 ‰ (2σ , $N = 3$) for the Elbaite 98144 and are accurate within uncertainties with published values (Leeman and Tonarini 2001; Míková et al. 2014; Marger et al. 2020). The B isotopic composition of the Inder inderborite is given in Table 1.

Single-crystal X-ray and neutron diffraction

To assess the quality of a range of crystals varying in size and shape, a KUMA-KM4 four-circle X-ray diffractometer was initially employed. This assessment aimed to select the better crystals for the collection of X-ray and neutron intensity data. Among those, a prismatic crystal (ca. $0.08 \times 0.130 \times 0.230$ mm³) of inderborite was selected for the X-ray intensity data collection at room temperature (ca. 293 K) with a Rigaku XtaLABSynergy-i X-ray diffractometer, equipped with a PhotonJet-i MoK α microfocus source and a HyPix-6000HE HPC detector, at the ESD-MI. Diffraction data were collected using an ad hoc routine in the CrysAlisPro suite (Rigaku-Oxford Diffraction 2019), maximizing the reciprocal space coverage and the quality of the intensity data, adopting an ω -scan strategy, 0.5° step size and an exposure time of 1 s per frame. A total number of 5759 Bragg reflections was collected up to $2\theta_{\text{max}}$ of 60° (with $-15 \leq h \leq +11$, $-9 \leq k \leq +9$ and $-25 \leq l \leq +26$), giving a metrically monoclinic unit-cell with $a = 12.1593(8)$, $b = 7.4084(6)$, $c = 19.230(2)$ Å, $\beta = 90.321(9)^\circ$, and $V = 1732.2(3)$ Å³; 1923 reflections were unique for symmetry ($R_{\text{int}} = 0.0248$, Laue class $2/m$) and 1832 with $I_o > 2\sigma(I_o)$. The reflection conditions were consistent with the space group $C2/c$. The intensity data were then corrected for Lorentz-polarization effects and X-ray absorption (with a semi-empirical strategy) using the ABSPACK routine implemented in the CrysAlisPro package (Rigaku-Oxford Diffraction 2019). The final intensity data were processed with the E-STATISTICS program (implemented in the WinGX package, Farrugia 1999), and the statistics of distributions of the normalized structure factors suggested that the structure of inderborite is centrosymmetric (at $>70\%$ likelihood). Additional details are given in the Online Materials CIF¹.

Low-temperature neutron diffraction data were collected on the four-circle diffractometer D9 at the Institut Laue-Langevin (ILL), Grenoble, France, using a single crystal of inderborite of $2.1 \times 1.8 \times 0.9$ mm³. The crystal was glued on an Al pin and placed on a close-circuit displacer device operated at 20(1) K (Archer and Lehmann 1986). The diffraction experiment was conducted with a wavelength of 0.8348 Å, obtained from a Cu(220) monochromator, and a small two-dimensional area detector. The data collection strategy was based on a series of ω -scans (for low- Q reflections) or ω - 2θ scans (for high- Q reflections), varying the ω -range as a function of the instrument resolution curve. A total of 4732 Bragg reflections was collected up to $2\theta_{\text{max}}$ of 114.9° (with $-20 \leq h \leq +19$, $0 \leq k \leq +14$ and $-4 \leq l \leq +25$), with $d_{\text{min}} = 0.498$ Å; 4509 reflections were unique for symmetry ($R_{\text{int}} = 0.0304$, Laue class $2/m$) and 3861 with $I_o > 2\sigma(I_o)$. Integrated intensities, corrected for Lorentz effects, were obtained with the Racer program (written by Clive Wilkinson and Garry McIntyre, ILL integration program suite). Absorption correction was also applied, considering the shape of the crystal and its chemical composition, using the ILL program Datap (last version of this program is available in the online SXTalSoft repository, <https://code.ill.fr/scientific-software/sxtalsoft>). The unit-cell was found to be metrically monoclinic, with $a = 12.047(2)$, $b = 7.399(1)$, $c = 19.157(3)$ Å, $\beta = 90.76(1)^\circ$, and $V = 1707.4(6)$ Å³, and the reflection conditions were consistent with the space group $C2/c$, confirming the previous findings based on the X-ray data. Additional details are given in the Online Materials CIF¹.

Two independent crystal-structure refinements were then performed on the basis of the X-ray (at 293 K) and neutron (at 20 K) intensity data using the

SHELXL-2018/3 software (Sheldrick 1997, 2008). Neutral X-ray scattering factors (from the *International Tables for X-ray Crystallography Vol. C*) of Mg, Ca, B, O, and H were used for the X-ray refinement, whereas their neutron scattering lengths were taken from Sears (1986). The secondary isotropic extinction effect was corrected by adopting the Larson's formalism (Larson 1967) in both refinements. The refinements were conducted with the starting structural model reported by Burns and Hawthorne (1994), without any H site. The first cycles of refinement were conducted with isotropic displacement parameters and then anisotropic till the convergence was achieved. However, due to the low temperature, the displacement parameters of the B sites in the neutron refinement were modest and quasi-isotropic; they were then modeled as isotropic in the next cycles. When convergence was achieved for both the data sets (i.e., neutron and X-ray), a series of residual peaks was found in the final difference-Fourier map of the nuclear or electron density: negative for the neutron refinement, positive for the X-ray one. As H has a negative neutron scattering length [i.e., $b_c(\text{H}) = -3.7409$ fm], the negative residual peaks observed in the difference-Fourier map of the nuclear density were assigned to the H sites for the next cycles of refinement. Eleven independent H sites were located, with realistic H-bonding geometry (in terms of O_D-H distances, O_D-H \cdots O_A angles and O_D \cdots O_A distances). Once all the H sites were modeled on the basis of the neutron data, the H population was then implemented in the X-ray refinement. Whereas the H sites were modeled with anisotropic displacement schemes in the neutron refinement, the H population was modeled with a unique isotropic displacement parameter in the X-ray one. When convergence was achieved for both the refinements, the variance-covariance matrix showed no significant correlation among the refined parameters, all the principal mean-square atomic displacement parameters were positive (including those for the H sites for the neutron refinement), and the residuals in the difference-Fourier maps (of nuclear or electron density) were not significant. The final $R_i(F)$ was 0.0695 (for 3861 obs./223 par.) for the neutron refinement and 0.0287 (for 1832 obs./173 par.) for the X-ray one. Some of the final atomic displacement ellipsoids of the neutron structure refinement at 20 K are significantly anisotropic, likely due to the inadequate correction of the extinction effects with the isotropic model of Larson (1967). Additional details of the structure refinements are listed in the Online Materials CIF¹; relevant interatomic distances and angles are listed in Table 2.

DISCUSSION AND IMPLICATIONS

The results of the multi-methodological approach used in this study confirm the general formula of inderborite previously reported in the literature: $\text{CaMg}[\text{B}_3\text{O}_3(\text{OH})_5]_2 \cdot 6\text{H}_2\text{O}$. However, based on the structural model, the correct form of the chemical formula of inderborite should be given as: $\text{CaMg}[\text{B}_3\text{O}_3(\text{OH})_5]_2(\text{H}_2\text{O})_4 \cdot 2\text{H}_2\text{O}$. The chemical analysis here performed showed that there are no major substituents of Ca, Mg, or B (Table 1), so that the real chemical composition of the inderborite from Inder is virtually identical to the ideal one, and the concentration of industrially critical elements (e.g., Li, Be, or REE) in inderborite is irrelevant (Table 1). The chemical purity of inderborite confirms the previous experimental findings on other hydrous borates, recently re-investigated using modern analytical protocols for chemical characterization. More specifically, colemanite $\{\text{Ca}[\text{B}_3\text{O}_4(\text{OH})_3] \cdot \text{H}_2\text{O}\}$ (Lotti et al. 2017, 2018, 2019), kurnakovite $\{\text{Mg}[\text{B}_3\text{O}_3(\text{OH})_5] \cdot 5\text{H}_2\text{O}\}$ (Gatta et al. 2019), kernite $\{\text{Na}_6[\text{B}_4\text{O}_5(\text{OH})_4]_3 \cdot 8\text{H}_2\text{O}\}$ (Gatta et al. 2020), meyerhofferite $\{\text{Ca}_2\text{B}_6\text{O}_6(\text{OH})_{10} \cdot 2\text{H}_2\text{O}\}$ (Gatta et al. 2022a), and also proberite $\{\text{CaNa}[\text{B}_3\text{O}_7(\text{OH})_4] \cdot 3\text{H}_2\text{O}\}$ (Gatta et al. 2022b) show no significant concentration of isomorphous substituents of the principal elements; as a result, their experimental formulas are basically identical to the ideal ones. The chemical purity of the hydrous borates was already reported as a common feature of this mineral population that does not depend on the nature of the deposit (e.g., Gatta et al. 2019, 2020, 2022b), but appears to be governed by the crystal structure selectivity and, likely, it is also the results of iterated dissolution and recrystallization in lacustrine environments, which could promote purification.

TABLE 2. Principal bond distances (Å) and angles (°) in the structure of inderborite, based on the X-ray refinement (data collected at 293 K) and neutron structure refinement (data collected at 20 K)

X-ray data (T = 293 K)					
Mg-O2 (x2)	2.083(1)	O2-H1	0.93(2)	O10-H8	0.92(2)
Mg-O8 (x2)	2.106(1)	O2-H1 ^a	0.96	O10-H8 ^a	0.95
Mg-O9 (x2)	2.092(1)	O2...O11	3.229(2)	O10...O4	2.803(2)
		H1...O11	2.45(2)	H8...O4	1.90(2)
Ca-O1 (x2)	2.392(1)	O2-H1...O11	141(2)	O10-H8...O4	165(2)
Ca-O3 (x2)	2.443(1)				
Ca-O6 (x2)	2.504(1)	O3-H2	0.91(2)	O10-H9	0.93(2)
Ca-O10 (x2)	2.450(1)	O3-H2 ^a	0.94	O10-H9 ^a	0.96
		O3...O7	2.863(2)	O10...O5	2.727(2)
B1-O1	1.438(2)	H2...O7	2.00(2)	H9...O5	1.85(2)
B1-O2	1.491(2)	O3-H2...O7	158(2)	O10-H9...O5	157(2)
B1-O3	1.477(2)			H8-O10-H9	112(2)
B1-O4	1.483(2)	O6-H3	0.93(2)		
		O6-H3 ^a	0.96	O11-H10	0.93(2)
B2-O1	1.443(2)	O6...O7	2.657(2)	O11-H10 ^a	0.96
B2-O5	1.487(2)	H3...O7	1.74(2)	O11...O9	3.107(2)
B2-O7	1.459(2)	O6-H3...O7	169(2)	H10...O9	2.40(3)
B2-O8	1.504(2)			O11-H10...O9	133(2)
		O7-H4	0.94(2)	O11...O6	3.166(2)
B3-O4	1.360(2)	O7-H4 ^a	0.97	H10...O6	2.48(2)
B3-O5	1.360(2)	O7...O3	2.826(1)	O11-H10...O6	131(2)
B3-O6	1.383(2)	H4...O3	1.90(2)		
		O7-H4...O3	166(2)	O11-H11	0.91(2)
O1-B1-O2	109.1(1)			O11-H11 ^a	0.94
O1-B1-O3	107.0(1)	O8-H5	0.92(2)	O11...O8	2.918(2)
O1-B1-O4	112.2(1)	O8-H5 ^a	0.95	H11...O8	2.06(2)
O2-B1-O3	112.1(1)	O8...O11	2.929(2)	O11-H11...O8	156(2)
O2-B1-O4	108.9(1)	H5...O11	2.06(2)	H10-O11-H11	102(2)
O3-B1-O4	107.5(1)	O8-H5...O11	158(2)		
O1-B2-O5	110.6(1)	O9-H6	0.93(2)		
O1-B2-O7	111.9(1)	O9-H6 ^a	0.96		
O1-B2-O8	109.1(1)	O9...O10	2.774(2)		
O5-B2-O7	108.9(1)	H6...O10	1.86(2)		
O5-B2-O8	107.6(1)	O9-H6...O10	170(2)		
O7-B2-O8	108.6(1)				
O4-B3-O5	123.8(1)	O9-H7	0.93(2)		
O4-B3-O6	120.0(1)	O9-H7 ^a	0.96		
O5-B3-O6	116.2(1)	O9...O11	2.816(2)		
		H7...O11	1.91(2)		
		O9-H7...O11	164(2)		
O2-Mg-O8 (x2)	86.55(4)	H6-O9-H7	100(2)		
O2-Mg-O8' (x2)	93.45(4)				
O2-Mg-O9 (x2)	88.30(5)				
O2-Mg-O9' (x2)	91.70(5)				
O8-Mg-O9 (x2)	89.85(5)				
O8-Mg-O9' (x2)	90.15(5)				

TABLE 2.—CONTINUED

Neutron data (T = 20 K)					
Mg-O2 (x2)	2.072(1)	O2-H1	0.956(3)	O10-H8	0.977(3)
Mg-O8 (x2)	2.111(1)	O2-H1 ^a	0.985	O10-H8 ^a	0.996
Mg-O9 (x2)	2.096(1)	O2...O11	3.223(2)	O10...O4	2.770(2)
		H1...O11	2.411(4)	H8...O4	1.807(3)
Ca-O1 (x2)	2.384(1)	O2-H1...O11	142.6(3)	O10-H8...O4	168.1(2)
Ca-O3 (x2)	2.439(1)				
Ca-O6 (x2)	2.485(1)	O3-H2	0.970(2)	O10-H9	0.982(3)
Ca-O10 (x2)	2.439(1)	O3-H2 ^a	0.988	O10-H9 ^a	0.999
		O3...O7	2.851(1)	O10...O5	2.723(1)
B1-O1	1.438(1)	H2...O7	1.921(3)	H9...O5	1.804(3)
B1-O2	1.492(2)	O3-H2...O7	159.6(2)	O10-H9...O5	154.2(2)
B1-O3	1.474(2)			H8-O10-H9	109.4(3)
B1-O4	1.483(1)	O6-H3	0.993(3)		
		O6-H3 ^a	1.009	O11-H10	0.966(3)
B2-O1	1.439(2)	O6...O7	2.618(2)	O11-H10 ^a	0.992
B2-O5	1.483(1)	H3...O7	1.633(3)	O11...O9	3.044(2)
B2-O7	1.464(1)	O6-H3...O7	170.6(2)	H10...O9	2.271(4)
B2-O8	1.505(2)			O11-H10...O9	136.4(3)
		O7-H4	0.975(3)		
B3-O4	1.362(1)	O7-H4 ^a	0.993	O11...O6	3.141(2)
B3-O5	1.359(1)	O7...O3	2.779(2)	H10...O6	2.485(4)
B3-O6	1.383(1)	H4...O3	1.817(3)	O11-H10...O6	125.0(3)
		O7-H4...O3	168.5(3)		
O1-B1-O2	109.1(1)			O11-H11	0.970(4)
O1-B1-O3	106.74(9)	O8-H5	0.970(3)	O11-H11 ^a	0.992
O1-B1-O4	112.08(8)	O8-H5 ^a	0.987	O11...O8	2.857(2)
O2-B1-O3	111.90(8)	O8...O11	2.917(2)	H11...O8	1.928(3)
O2-B1-O4	108.99(8)	H5...O11	1.976(3)	O11-H11...O8	159.8(3)
O3-B1-O4	108.1(1)	O8-H5...O11	162.8(2)	H10-O11-H11	106.1(3)
O1-B2-O5	111.3(1)				
O1-B2-O7	111.41(9)	O9-H6	0.986(3)		
O1-B2-O8	108.78(8)	O9-H6 ^a	1.003		
O5-B2-O7	108.66(8)	O9...O10	2.760(2)		
O5-B2-O8	107.59(9)	H6...O10	1.790(3)		
O7-B2-O8	109.0(1)	O9-H6...O10	167.0(3)		
		O9-H7	0.973(3)		
O4-B3-O5	123.20(9)	O9-H7 ^a	0.990		
O4-B3-O6	120.3(1)	O9...O11	2.811(2)		
O5-B3-O6	116.45(9)	H7...O11	1.857(3)		
		O9-H7...O11	166.2(3)		
O2-Mg-O8 (x2)	86.10(4)	H6-O9-H7	105.4(3)		
O2-Mg-O8' (x2)	93.90(4)				
O2-Mg-O9 (x2)	87.57(5)				
O2-Mg-O9' (x2)	92.43(5)				
O8-Mg-O9 (x2)	89.58(4)				
O8-Mg-O9' (x2)	90.42(4)				

^a Bond distance corrected for "riding motion" effect, according to Busing and Levy (1964).

The in situ B isotopic composition of the Inder inderborite is relatively homogeneous and significantly enriched in the ¹¹B isotope. As observed in this study, single spot analyses along a rim-core-rim profile parallel to the *c*-axis report identical B isotope composition within error (from +34.89 ± 0.53 to +35.61 ± 0.66‰; error expressed as 2σ), thus providing a weighted mean δ¹¹B of +35.15 ± 0.49‰ (2σ, N = 6) (Table 1). Such a δ¹¹B value falls within the range of values in which the source of boron is ascribable to marine reservoirs, rather than to terrestrial ones (e.g., Swihart et al. 1986; Hussain et al. 2021 and references therein). At the Inder deposits, the borates occur as veins at the top of a large salt dome complex, and are considered as the effect of remobilization and concentration during the intrusion of the salt dome itself (Helvacı 2005).

The X-ray and neutron structure refinements of this study consistently confirm the general structural model of inderborite previously reported by Burns and Hawthorne (1994). The principal building block unit of the structure is a [B₃O₃(OH)₃]²⁻ ring, usually represented by the descriptor <Δ2□> [where Δ stands

for a Bφ₃ unit and □ for a Bφ₄ tetrahedron; φ is O²⁻, OH⁻, or H₂O (Burns et al. 1995; Hawthorne 2012)] or 3:1Δ+2T (Christ and Clark 1977), consisting of 2Bφ₄ tetrahedra [i.e., BO₂(OH)₂], B-ion in *sp*³ electronic configuration] and one planar-triangular Bφ₃ group (i.e., BO₂OH, B-ion in *sp*² electronic configuration) (Fig. 1; Table 2). In the [B₃O₃(OH)₃]²⁻ ring, all the oxygen atoms that are not shared between two boron atoms are protonated. The building units share corners with the Caφ₈ polyhedra [i.e., antiprism CaO₂(OH)₄(OH₂)₂] and Mgφ₆ octahedra [i.e., Mg(OH)₄(OH₂)₂], forming hetero-polyhedral sheets parallel to (100) (Fig. 1). Subsequent hetero-polyhedral sheets are mutually connected only by H-bonding interactions, even mediated by the zeolitic (i.e., "interstitial") H₂O molecules. This structural feature occurs even in other hydrous borates, e.g., kurnakovite (Gatta et al. 2019), and well explains the good cleavage on {100} usually observed in inderborite crystals.

A careful analysis of the X-ray and neutron structural models obtained in this study shows that (numerical data from the neutron refinement):

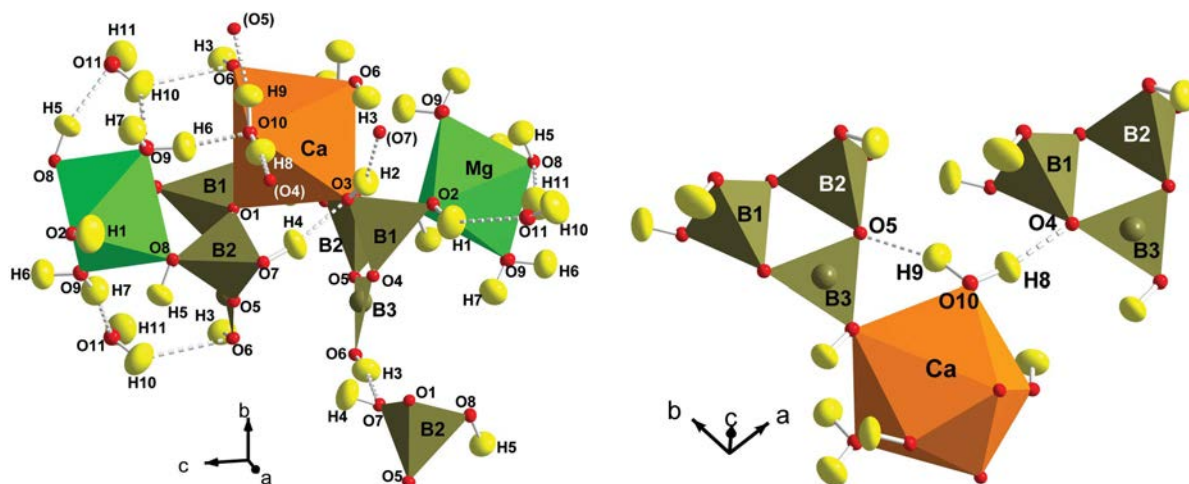


FIGURE 2. The complex and pervasive H-bonding scheme into the crystal structure of inderborite, based on the neutron structure refinement of this study (data collected at 20 K). Details are listed in Table 2. Displacement ellipsoid probability factor: 90%. (Color online.)

(1) The unique triangular group (i.e., B_3O_2OH) exhibits an almost ideal configuration, with $\Delta(B_3O)_\text{max} \sim 0.02 \text{ \AA}$ (i.e., where Δ is the difference between the longest and the shortest B-O refined distances), average O-B-O angles of 120° (ranging between $116.2\text{--}123.8^\circ$) and aplanarity $<0.9^\circ$ (here defined as the average angle described by the plane on which the three-oxygen sites lie and each of the three independent B-O_n vectors) (Online Materials CIF¹; Table 2). The two independent tetrahedral units [i.e., $B_1O_2(OH)_2$ and $B_2O_2(OH)_2$; Fig. 2; Table 2] are slightly distorted, with: $\Delta(B_1-O)_\text{max} \sim 0.05 \text{ \AA}$, $\langle O-B_1-O \rangle \sim 109.5^\circ$, and $\Delta(O-B_1-O)_\text{max} \sim 5.3^\circ$; $\Delta(B_2-O)_\text{max} \sim 0.06 \text{ \AA}$, $\langle O-B_2-O \rangle \sim 109.5^\circ$, and $\Delta(O-B_2-O)_\text{max} \sim 4.3^\circ$. The longest distances (i.e., B1-O2 and B2-O8) are ascribable to the B-OH bonds (Online Materials CIF¹; Table 2).

(2) The Mg-octahedron, in which Mg^{2+} is coordinated by four hydroxyl groups and two H_2O molecules [i.e., $Mg(OH)_4(OH_2)_2$], is only slightly distorted, with $\Delta(Mg-O)_\text{max} \sim 0.04 \text{ \AA}$, $\langle O-Mg-O \rangle = 90.0^\circ$ (ranging between $86.1^\circ\text{--}93.9^\circ$) and $\Delta(O-Mg-O)_\text{max} \sim 5.2^\circ$. As expected, the Ca-polyhedron (in an antiprism configuration), in which the cation is coordinated by two O, four OH-groups and two H_2O molecules [i.e., $CaO_2(OH)_4(OH_2)_2$], is significantly distorted with $Ca-O_\text{min} \sim 2.38$ and $Ca-O_\text{max} \sim 2.48 \text{ \AA}$ (Figs. 1 and 2; Table 2; Online Materials CIF¹).

(3) In the structure of inderborite, three crystallographically independent H_2O molecule sites occur: H6-O9-H7 (bonded to Mg), H8-O10-H9 (bonded to Ca), and H10-O11-H11 (the “zeolitic” molecule) (Table 2). All the refined O-H bond distances were corrected for the “riding motion effect,” following the protocol of Busing and Levy (1964), with final distances ranging between 0.990 and 1.003 \AA (Table 2). Two of the independent H_2O molecules show an almost ideal geometrical configuration, with $H_6-O_9-H_7 = 105.5(3)^\circ$ and $H_{10}-O_{11}-H_{11} = 106.1(3)^\circ$, whereas the third one shows a “stretched” configuration with $H_8-O_{10}-H_9 = 109.4(3)^\circ$. The H-bonding scheme of the three H_2O molecules is the following:

- for H6-O9-H7, the acceptors are the oxygen sites O10 and O11, with $O_9-H_6 \cdots O_{10} = 167.0(3)^\circ$ [$O_9 \cdots O_{10} = 2.760(2) \text{ \AA}$] and $O_9-H_7 \cdots O_{11} = 166.2(3)^\circ$ [$O_9 \cdots O_{11} = 2.811(2) \text{ \AA}$];

- for H8-O10-H9, the acceptors are the oxygen sites O4 and O5, with $O_{10}-H_8 \cdots O_4 = 168.1(2)^\circ$ [$O_{10} \cdots O_4 = 2.770(2) \text{ \AA}$] and $O_{10}-H_9 \cdots O_5 = 154.2(2)^\circ$ [$O_{10} \cdots O_5 = 2.723(1) \text{ \AA}$];
- for H10-O11-H11, the H-bonding scheme is more complex, with bifurcated configurations for H10: the acceptors are the oxygen sites O6 and O9 (via H10), and O8 (via H11), with $O_{11}-H_{10} \cdots O_6 = 125.0(3)^\circ$ [$O_{11} \cdots O_6 = 3.141(2) \text{ \AA}$], $O_{11}-H_{10} \cdots O_9 = 136.4(3)^\circ$ [$O_{11} \cdots O_9 = 2.271(4) \text{ \AA}$], and $O_{11}-H_{11} \cdots O_8 = 159.8(3)^\circ$ [$O_{11} \cdots O_8 = 2.857(2) \text{ \AA}$] (Fig. 2; Table 2).

Except the bifurcated H-bond of the zeolitic H_2O molecule, mediated by the H10 proton, (i.e., $O_{11}-H_{10} \cdots O_6$ and $O_{11}-H_{10} \cdots O_9$), all the other $O_D-H \cdots O_A$ angles range between 154° and 168° , with $O_D \cdots O_A$ distances between 2.72 and 2.86 \AA , approaching a configuration energetically favorable (Table 2). The bifurcated configuration of the H-bonding scheme mediated by H10 is the only possible, considering all the potential acceptor sites with $O_D \cdots O_A$ and $H \cdots O_A$ distances compatible for a potential H-bond interaction.

The “stretched” configuration of the H8-O10-H9 molecule is the effect of the location of the two acceptor sites: O4 and O5 comprise, along with the donor O10, a significantly obtuse $O_4 \cdots O_{10} \cdots O_5$ angle of about 120.8° , forcing the H8-O10-H9 molecule to have a H-O-H angle of about 109.4° to keep the $O_4 \cdots H_8-O_{10}-H_9 \cdots O_5$ bonding scheme (Fig. 2). Often, in minerals, the H-O-H geometry tends to deviate from the ideal configuration in response to the H-bonding environment, forcing the molecules to have “compressed” or “stretched” forms (e.g., Gatta et al. 2008, 2021).

The hydroxyl groups (i.e., O2-H, O3-H, O6-H, O7-H, and O8-H; Online Materials CIF¹; Table 2), in the structure of inderborite, show O-H distances, corrected for “riding motion effect,” ranging between 0.98–1.01 \AA , $O_D \cdots O_A$ distances between 2.62–3.22 \AA , and $O_D-H \cdots O_A$ angles between $141\text{--}169^\circ$.

Overall, 10 out of 11 independent oxygen sites in the structure of inderborite are involved in H-bonds as donors or acceptors (Table 2), and this reflects the pervasive effect of the H-bonding

network. According to Burns and Hawthorne (1994), the role played by the complex H-bond network is expected to be substantial in the stability of the crystalline edifice, having effects within the single hetero-polyhedral sheet (i.e., O7-H4···O3, O9-H6···O10, and O10-H9···O5; Fig. 2; Table 2), between subsequent sheets (i.e., O3-H2···O7, O6-H3···O7, and O10-H8···O4; Fig. 2; Table 2), and in the bonding with the interstitial zeolitic H₂O molecules (i.e., O11-H10···O9, O11-H10···O6, and O11-H11···O8; Fig. 2; Table 2). It is worth noting that the atomic positions of the H sites obtained in this study by neutron diffraction are similar, but not identical, to those reported by Burns and Hawthorne (1994), in which soft constraints were imposed on the O-H distances (i.e., 0.96 Å) in their structure refinement. As a result, the geometry of the H₂O molecules is different: for example, our neutron refinement provides a H6-O9-H7 angle of 105.4(3)° (Table 2), whereas the counterpart based on the X-ray refinement of Burns and Hawthorne (1994) is 100(3)°. A similar limitation concerning the location of the H sites is also in the X-ray structural model of this study based on the use of a modern device. This further supports the important role of neutron diffraction in providing better structural models of hydrous materials when compared to X-ray diffraction, especially when a complex and pervasive H-bonding network occurs in the crystalline edifice.

(4) The Raman spectrum of inderborite reported in the RRUFF database (<https://rruff.info/Inderborite>) and in the collection of Chukanov (2014) shows at least seven independent peaks in the O-H stretching region (i.e., 3000–3700 cm⁻¹). This finding supports the complex H-bonding scheme described in this study.

The experimental findings about the complex and pervasive nature of the H-bonding scheme in inderborite confirm the previous results for other hydrous borates (e.g., Lotti et al. 2018, 2019; Gatta et al. 2019, 2020, 2022a, 2022b). We expect that a thermal, compressional or chemical perturbation of the H-bonding scheme would easily lead to a phase transition, or even to a decomposition of this mineral. At present, the behavior of inderborite at non-ambient conditions is entirely unknown.

In the framework of a long-term project on the potential utilization of natural borates as B-rich aggregates in concretes, acting as radiation-shielding materials for the pronounced ability of ¹⁰B to absorb thermal neutrons, we have recently re-investigated the high/low-temperature and high-pressure crystal-chemistry of a series of hydrous borates, bracketing their phase stability fields and the potential destabilization factors governed by the crystal structure (e.g., Lotti et al. 2017, 2018; Pagliaro et al. 2021; Comboni et al. 2020a, 2020b, 2022, 2023). Inderborite, with its high-B content (ca. 41 wt% B₂O₃), could potentially be a good candidate as a B-rich aggregate in concretes. To the best of our knowledge, the solubility and the effects in the hardening stage of inderborite in Portland or in Sorel cement pastes are still unknown. Inderborite does not contain the alkali elements, i.e., Na and K, which could potentially generate the so-called “alkali-silica reactions,” ASR, deleterious for the durability of Portland cements.

ACKNOWLEDGMENTS

The authors thank the Institut Laue-Langevin (Grenoble, France) for the allocation of the beamtime (DOI: 10.5291/ILL-DATA.DIR-264) and the COSPECT UNITECH platform of the University of Milan for the X-ray diffraction and EPMA-

WDS investigations. Gianluca Sessa is thanked for technical assistance during LA-MC-ICP-MS sessions. W. Depmeier, an anonymous reviewer, and the Associate Editor, O. Tschauer, are warmly thanked for the revision of the manuscript.

FUNDING

G.D.G., E.C., T.B., and D.C. acknowledge the support of the Italian Ministry of Education (MUR) through the projects “Dipartimenti di Eccellenza 2023–2027: Le Georisorse per la transizione ecologica e lo sviluppo territoriale” and “PRIN2017—Mineral reactivity, a key to understand large-scale processes” (2017L83S77).

REFERENCES CITED

- Archer, J. and Lehmann, M.S. (1986) A simple adjustable mount for a two-stage cryorefrigerator on an Eulerian cradle. *Journal of Applied Crystallography*, 19, 456–458, <https://doi.org/10.1107/S0021889886088957>.
- Burns, P.C. and Hawthorne, F.C. (1994) Structure and hydrogen bonding in inderborite, a heteropolyhedral sheet structure. *Canadian Mineralogist*, 32, 533–539.
- Burns, P.C., Grice, J.D., and Hawthorne, F.C. (1995) Borate minerals; I, Polyhedral clusters and fundamental building blocks. *Canadian Mineralogist*, 33, 1131–1151.
- Busing, W.R. and Levy, H.A. (1964) The effect of thermal motion on the estimation of bond lengths from diffraction measurements. *Acta Crystallographica*, 17, 142–146, <https://doi.org/10.1107/S0365110X64000408>.
- Carter, R.S., Palevsky, H., Myers, V.W., and Hughes, D.J. (1953) Thermal neutron absorption cross sections of boron and gold. *Physical Review*, 92, 716–721, <https://doi.org/10.1103/PhysRev.92.716>.
- Catanzaro, F., Champion, C., Garner, E., Marinenko, G., Sappenfield, K., and Shields, W. (1970) Boric acid: Isotopic and assay standard reference materials. National Bureau of Standards Special Publication, 260, 1–70.
- Christ, C.L. and Clark, J.R. (1977) A crystal-chemical classification of borate structures with emphasis on hydrated borates. *Physics and Chemistry of Minerals*, 2, 59–87, <https://doi.org/10.1007/BF00307525>.
- Chukanov, N.V. (2014) *Infrared Spectra of Mineral Species: Extended library*, 1726 p. Springer.
- Comboni, D., Pagliaro, F., Gatta, G.D., Lotti, P., Milani, S., Merlini, M., Battiston, T., Glazyrin, K., and Liermann, H.-P. (2020a) High-pressure behavior and phase stability of Na₂B₄O₆(OH)·3H₂O (kernite). *Journal of the American Ceramic Society*, 103, 5291–5301, <https://doi.org/10.1111/jace.17185>.
- Comboni, D., Pagliaro, F., Gatta, G.D., Lotti, P., Battiston, T., Garbarino, G., and Hanfland, M. (2020b) High-pressure behaviour and phase stability of Ca₂B₆O₆(OH)₁₀·2(H₂O) (meyerhofferite). *Physics and Chemistry of Minerals*, 47, 50, <https://doi.org/10.1007/s00269-020-01117-3>.
- Comboni, D., Battiston, T., Pagliaro, F., Lotti, P., Gatta, G.D., and Hanfland, M. (2022) High-pressure behaviour and atomic-scale deformation mechanisms in inyoite, CaB₃O₃(OH)₅·4H₂O. *Physics and Chemistry of Minerals*, 49, 4, <https://doi.org/10.1007/s00269-021-01173-3>.
- Comboni, D., Poreba, T., Battiston, T., Hanfland, M., and Gatta, G.D. (2023) On the anomalous high-pressure phase transition of inderite, MgB₃O₃(OH)₅·5H₂O. *Solid State Sciences*, 140, 107187, <https://doi.org/10.1016/j.solidstatessciences.2023.107187>.
- Farrugia, L.J. (1999) WinGX suite for small-molecule single-crystal crystallography. *Journal of Applied Crystallography*, 32, 837–838, <https://doi.org/10.1107/S0021889899006020>.
- Fleischer, M. (1943) New mineral names. *American Mineralogist*, 28, 282–284.
- Gatta, G.D., Rotiroli, N., McIntyre, G.J., Guastoni, A., and Nestola, F. (2008) New insights into the crystal chemistry of epididymite and eudidymite from Malosa, Malawi: A single-crystal neutron diffraction study. *American Mineralogist*, 93, 1158–1165, <https://doi.org/10.2138/am.2008.2965>.
- Gatta, G.D., Guastoni, A., Lotti, P., Guastella, G., Fabelo, O., and Fernandez-Diaz, M.T. (2019) A multi-methodological study of kernakovite: A potential B-rich aggregate. *American Mineralogist*, 104, 1315–1322, <https://doi.org/10.2138/am-2019-7072>.
- Gatta, G.D., Guastoni, A., Lotti, P., Guastella, G., Fabelo, O., and Fernandez-Diaz, M.T. (2020) A multi-methodological study of kernite, a mineral commodity of boron. *American Mineralogist*, 105, 1424–1431, <https://doi.org/10.2138/am-2020-7433>.
- Gatta, G.D., Hradil, K., and Meven, M. (2021) Where is the hydrogen? *Elements*, 17, 163–168, <https://doi.org/10.2138/gselements.17.3.163>.
- Gatta, G.D., Guastella, G., Capelli, S., Comboni, D., and Guastoni, A. (2022a) On the crystal-chemistry of meyerhofferite, CaB₃O₃(OH)·H₂O. *Physics and Chemistry of Minerals*, 49, 22, <https://doi.org/10.1007/s00269-022-01199-1>.
- Gatta, G.D., Cannao, E., Gagliardi, V., and Fabelo, O. (2022b) Reinvestigation of proberite, CaNa[B₃O₃(OH)₄]·3H₂O, a mineral commodity of boron. *American Mineralogist*, 107, 1378–1384, <https://doi.org/10.2138/am-2022-8086>.
- Gorshkov, G.S. (1941) A new mineral from the region of Lake Inder. *Comptes Rendus (Doklady) de l'Académie des Sciences de l'URSS*, 33, 254–256.
- Griffin, W.L., Powell, W., Pearson, N.J., and O'Reilly, S.Y. (2008) GLITTER: Data reduction software for laser ablation ICP-MS. *Laser Ablation-ICP-MS in the Earth Sciences: Current practices and outstanding issues*, 308–311.

- Mineralogical Association of Canada.
- Hawthorne, F.C. (2012) A bond-topological approach to theoretical mineralogy: Crystal structure, chemical composition and chemical reactions. *Physics and Chemistry of Minerals*, 39, 841–874, <https://doi.org/10.1007/s00269-012-0538-4>.
- Helvacı, C. (2005) Borates. In R.C. Selley, L.R.M. Cocks, and I.R. Plimer, Eds., *Encyclopedia of Geology*, 3, 510–522. Elsevier.
- Hussain, S.A., Han, F.Q., Ma, Z., Hussain, A., Mughal, M.S., Han, J., Alhassan, A., and Widory, D. (2021) Unraveling sources and climate conditions prevailing during the deposition of Neoproterozoic evaporites using coupled chemistry and boron isotope compositions ($\delta^{11}\text{B}$): The example of the Salt Range, Punjab, Pakistan. *Minerals*, 11, 161, <https://doi.org/10.3390/min11020161>.
- Ikornikova, M.V. and Godlevsky, M.N. (1941) The new borate: Metahydroborate. *Comptes rendus de l'académie des sciences de l'U.R.S.S.*, 33, 257–258.
- Jochum, K.P., Weis, U., Stoll, B., Kuzmin, D., Yang, Q., Raczek, I., Jacob, D.E., Stracke, A., Birbaum, K., Frick, D.A., and others. (2011) Determination of reference values for NIST SRM 610–617 glasses following ISO guidelines. *Geostandards and Geoanalytical Research*, 35, 397–429, <https://doi.org/10.1111/j.1751-908X.2011.00120.x>.
- Kurkutova, E., Rumanova, I., and Belov, N. (1966) Crystal structure of inderborite. *Soviet Physics, Doklady*, 10, 808–810.
- Larson, A.C. (1967) Inclusion of secondary extinction in least-squares calculations. *Acta Crystallographica*, 23, 664–665, <https://doi.org/10.1107/S0365110X67003366>.
- Leeman, W.P. and Tonarini, S. (2001) Boron isotopic analysis of proposed borosilicate mineral reference samples. *Geostandards Newsletter*, 25, 399–403, <https://doi.org/10.1111/j.1751-908X.2001.tb00614.x>.
- Lotti, P., Gatta, G.D., Comboni, D., Guastella, G., Merlini, M., Guastoni, A., and Liermann, H.P. (2017) High-pressure behavior and *P*-induced phase transition of $\text{CaB}_2\text{O}_4(\text{OH}) \cdot \text{H}_2\text{O}$ (colemanite). *Journal of the American Ceramic Society*, 100, 2209–2220, <https://doi.org/10.1111/jace.14730>.
- Lotti, P., Gatta, G.D., Demitri, N., Guastella, G., Rizzato, S., Ortenzi, M.A., Magrini, F., Comboni, D., Guastoni, A., and Fernandez-Diaz, M.T. (2018) Crystal-chemistry and temperature behavior of the natural hydrous borate colemanite, a mineral commodity of boron. *Physics and Chemistry of Minerals*, 45, 405–422, <https://doi.org/10.1007/s00269-017-0929-7>.
- Lotti, P., Comboni, D., Gigli, L., Carlucci, L., Mossini, E., Macerata, E., Mariani, M., and Gatta, G.D. (2019) Thermal stability and high-temperature behavior of the natural borate colemanite: An aggregate in radiation-shielding concretes. *Construction & Building Materials*, 203, 679–686, <https://doi.org/10.1016/j.conbuildmat.2019.01.123>.
- Marger, K., Harlaux, M., Rielli, A., Baumgartner, L.P., Dini, A., Dutrow, B.L., and Bouvier, A.S. (2020) Development and re-evaluation of tourmaline reference materials for in situ measurement of boron δ values by secondary ion mass spectrometry. *Geostandards and Geoanalytical Research*, 44, 593–615, <https://doi.org/10.1111/ggr.12326>.
- Marschall, H.R., Ludwig, T., Altherr, R., Kalt, A., and Tonarini, S. (2006) Syros metasomatic tourmaline: Evidence for very high- $\delta^{11}\text{B}$ fluids in subduction zones. *Journal of Petrology*, 47, 1915–1942, <https://doi.org/10.1093/ptrology/egl031>.
- Miková, J., Košler, J., and Wiedenbeck, M. (2014) Matrix effects during laser ablation MC ICP-MS analysis of boron isotopes in tourmaline. *Journal of Analytical Atomic Spectrometry*, 29, 903–914, <https://doi.org/10.1039/c3ja50241d>.
- Pagliari, F., Lotti, P., Battiston, T., Comboni, D., Gatta, G.D., Cámara, F., Milani, S., Merlini, M., Glazyrin, K., and Liermann, H.-P. (2021) Thermal and compressional behavior of the natural borate kurnakovite, $\text{MgB}_2\text{O}_3(\text{OH})_2 \cdot 5\text{H}_2\text{O}$. *Construction & Building Materials*, 266, 121094, <https://doi.org/10.1016/j.conbuildmat.2020.121094>.
- Palmer, M.R. and Swihart, G.H. (1996) Boron isotope geochemistry: An overview. In L.M. Anovitz and E.S. Grew, Eds., *Boron: Mineralogy, Petrology, and Geochemistry*, 33, p. 709–744. Review in *Mineralogy, Mineralogical Society of America*, Chantilly, Virginia.
- Pekov, I.V. (1998) *Minerals First Discovered on the Territory of the Former Soviet Union*, 369 p. Ocean Pictures Ltd.
- Pekov, I.V. and Abramov, D.V. (1993) Boron deposit of the Inder and its minerals. *World of Stones*, 1, 23–30.
- Rauch, H. and Waschkowski, W. (2002) Neutron scattering lengths. In A.J. Dianoux and G. Lander, Eds., *Neutron Data Booklet*, 1st ed., p. 1–18. Institut Laue Langevin.
- Rigaku-Oxford Diffraction (2019) *CrysAlisPro: Single crystal X-ray diffraction data collection and processing software*. Rigaku Corporation (<https://www.rigaku.com/products/crystallography/crystalis>).
- Sears, V.F. (1986) Neutron scattering lengths and cross-sections. In K. Sköld and D.L. Price, Eds., *Neutron Scattering, Methods of Experimental Physics*, 23a, 521–550. Academic Press.
- Sheldrick, G.M. (1997) SHELXL-97. Programs for crystal structure determination and refinement. University of Göttingen.
- (2008) A short history of SHELX. *Acta Crystallographica A*, 64, 112–122, <https://doi.org/10.1107/S0108767307043930>.
- Swihart, G.H., Moore, P.B., and Callis, E.L. (1986) Boron isotopic composition of marine and nonmarine evaporite borates. *Geochimica et Cosmochimica Acta*, 50, 1297–1301, [https://doi.org/10.1016/0016-7037\(86\)90413-8](https://doi.org/10.1016/0016-7037(86)90413-8).
- Tonarini, S., Pennisi, M., Adorni-Braccesi, A., Dini, A., Ferrara, G., Gonfiantini, R., Wiedenbeck, M., and Gröning, M. (2003) Intercomparison of boron isotope and concentration measurements. Part I: Selection, preparation and homogeneity tests of the intercomparison materials. *Geostandards Newsletter*, 27, 21–39, <https://doi.org/10.1111/j.1751-908X.2003.tb00710.x>.
- Wilson, S.A. (2018) G-probe 20 Summary Report. International Association of Geoanalysts, G probe 20, 1–13 p.
- Wu, S., Yang, Y., Jochum, K.P., Romer, R.L., Glodny, J., Savov, I.P., Agostini, S., De Hoog, J.C.M., Peters, S.T.M., Kronz, A., and others. (2021) Isotopic compositions (Li-B-Si-O-Mg-Sr-Nd-Hf-Pb) and $\text{Fe}^{2+}/\Sigma\text{Fe}$ ratios of three synthetic andesite glass reference materials (ARM-1, ARM-2, ARM-3). *Geostandards and Geoanalytical Research*, 45, 719–745, <https://doi.org/10.1111/ggr.12399>.

MANUSCRIPT RECEIVED AUGUST 21, 2023

MANUSCRIPT ACCEPTED OCTOBER 3, 2023

ACCEPTED MANUSCRIPT ONLINE OCTOBER 12, 2023

MANUSCRIPT HANDLED BY OLIVER TSCHAUNER

Endnote:

¹Deposit item AM-24-79162. Online Materials are free to all readers. Go online, via the table of contents or article view, and find the tab or link for supplemental materials. The CIF has been peer-reviewed by our Technical Editors.